

Current production in ring condensates with a weak link

Axel Pérez-Obiol,¹ Juan Polo ², and Taksu Cheon ¹

¹Laboratory of Physics, Kochi University of Technology, Tosa Yamada, Kochi 782-8502, Japan

²Quantum Systems Unit, Okinawa Institute of Science and Technology Graduate University, Onna, Okinawa 904-0495, Japan



(Received 27 July 2020; revised 19 November 2020; accepted 19 November 2020; published 3 December 2020)

We consider attractive and repulsive condensates in a ring trap stirred by a weak link, and analyze the spectrum of solitonic trains dragged by the link, by means of analytical expressions for the wave functions, energies, and currents. The precise evolution of current production and destruction in terms of defect formation in the ring and in terms of stirring is studied. We find that any excited state can be coupled to the ground state through two proposed methods: either by adiabatically tuning the link's strength and velocity through precise cycles which avoid the critical velocities and thus unstable regions or by keeping the link still while setting an auxiliary potential and imprinting a nonlinear phase as the potential is turned off. We also analyze hysteresis cycles through the spectrum of energies and currents.

DOI: [10.1103/PhysRevA.102.063302](https://doi.org/10.1103/PhysRevA.102.063302)

I. INTRODUCTION

Condensates in ring geometries present a wealth of superfluid and nonlinear effects and yield the potential for the development of atomtronic devices [1]. Production and decay of supercurrents, supersonic flow, hysteresis cycles, and the ability to sustain solitonic solutions have been widely studied theoretically and experimentally [2–12]. The production and control of supercurrents is a crucial step towards future quantum devices. For instance, the atomic analog of the superconducting quantum interference device, which was realized experimentally in Ref. [13], is based on the stirring of a weak link across a condensate trapped in a ring geometry. This process has been extensively investigated and it has been shown capable to produce superposition of current states [10,14].

One dimensional rings offer the opportunity to analyze the spectrum much more precisely, and to tackle new effects which are in general masked by higher dimensional dynamics, such as non-vortex-antivortex phase slips [15]. Experimentally, the production of currents can be induced by a rotating weak link. The link produces a low density region and can be rotated to stir the condensate and produce superfluid currents [13,15–17]. Alternatively, a phase can be directly imprinted on the condensate [18,19]. In the latter case, however, Bose-Josephson Junction (BJJ) oscillations are found in the case of a large enough defect or a small enough nonlinearity [20].

With the aim to better understand the behavior of currents in ring condensates, various works have analyzed these systems in the mean field limit and at zero temperature. Current dynamics have been studied through either a rotational drive [21], through the interaction between symmetry breaking potentials and rotation such as in lattice rings [22–24], or through rotating defects [25–27]. Solutions of the Gross-Pitevskii equation (GPE) for a 1D ring, in the free case and with various sets of potentials, have been established by analyzing its spectrum either numerically and/or through the use of Jacobi

elliptic functions [28–34]. The spectrum for a moving link and repulsive interactions was analyzed thoroughly in [35]. Studying how current states are coupled to either the ground state or dark solitonic states, which are found to trigger phase slips, has proven essential to understand production and decay of currents, and how to build more robust states.

In this paper, we complement previous studies by determining and describing the spectrum and critical velocities for both attractive and repulsive stirred condensates. The use of analytical solutions releases us from the limitation to study the ground state, and also allows us to explore the current dynamics of stirred excited states. We focus on three main mechanisms for current production: adiabatic excitation, hysteresis, and phase imprinting. In the case of adiabatic excitation, we distinguish two types of stirrings, one which starts at zero velocity, and another in which the link is set while rotating, allowing for production of larger currents. Each mechanism is thoroughly analyzed through the spectrum of energies and currents. We provide explicit protocols to produce the first excited states, and compare the cases for repulsive and attractive interactions; to the best of our knowledge, this is the first time this analysis has been performed for attractive interactions.

This article is organized as follows. The main features of the spectrum are laid out in Sec. II, and details are given in Appendix. In Sec. III, we analyze how currents depend on the link's velocity and strength, through regular stirring, in Sec. III A, and through a set of adiabatic cycles which are able to couple any stationary current to the ground state, in Sec. III B. We also connect the energy and current spectra to a set of hysteresis cycles in Sec. III C. In Sec. III D, we present an alternative method for stable current production in rings with weak links. This protocol does not involve the movement of the link, but setting an auxiliary potential and phase imprinting a nonlinear slope, so that no BJJ oscillations are found. We conclude in Sec. IV.

II. EXACT SPECTRUM OF A STIRRED BEC

Within the mean field limit, and at zero temperature, the condensate wave function on a ring $\psi(\theta, t)$ is determined by the Gross-Pitaevskii equation (GPE),

$$i\hbar \partial_t \psi(\theta, t) = -\frac{\hbar^2}{2MR^2} \partial_\theta^2 \psi(\theta, t) + g|\psi(\theta, t)|^2 \psi(\theta, t) + V(\theta, t)\psi(\theta, t), \quad (1)$$

with $\theta \in [0, 2\pi)$, g the reduced 1D coupling, and $V(\theta)$ an external potential. From here onwards we work in natural units, where the ring's radius R , the atomic mass M , and \hbar are $R = M = \hbar = 1$, and in the frame of reference comoving with the link. In this frame of reference, where the link is modeled by a static Dirac delta, the stationary wave function $\phi(\theta)$ and chemical potential μ are fully determined by

$$-\frac{1}{2}\phi''(\theta) + g|\phi(\theta)|^2\phi(\theta) = \mu\phi(\theta), \quad (2)$$

$$\phi(0) - e^{i2\pi\Omega}\phi(2\pi) = 0, \quad (3)$$

$$\phi'(0) - e^{i2\pi\Omega}\phi'(2\pi) = 2\alpha\phi(0), \quad (4)$$

where α and Ω are the link's strength and velocity, and where the wave function is normalized to $\int_0^{2\pi} d\theta |\phi(\theta)|^2 = 1$. This framework allows us to use analytical expressions for the wave functions, chemical potentials, and currents. It takes advantage of the elliptic functions, which appear as solutions of the nonlinear Schrödinger equation. These functions are in general useful in 1D GPE models with point interactions, see, for example, Refs. [29,36], or in developing solvable models which either generalize the GPE to a higher-order nonlinear Schrödinger equation [37], or apply Darboux transformations to find solvable potentials [38]. In our case, the solutions are those of the free GPE and the moving potential is relegated to applying in them boundary conditions (3) and (4). In particular, the chemical potential is given by

$$\mu(k, m) = \frac{1}{4\pi}(3g + 2k^2(m-2) + 3k\eta), \quad (5)$$

with $k \geq 0$ and $m \in [0, 1]$ the frequency and elliptic modulus of the Jacobi solution, and $\eta = E[\text{JA}(k(2\pi - \theta_0), m), m] + E[\text{JA}(k\theta_0, m), m]$. θ_0 is a shift depending on k and m such that the wave is continuous at $\theta = 0, 2\pi$, E is the elliptic integral of the second kind, and JA the Jacobi amplitude. Equations (3)–(5) then provide $\alpha(k, m)$, $\Omega(k, m)$, and $\mu(k, m)$, from which we compute $\mu(\alpha, \Omega)$. The precise relationship between the frequency and the elliptic modulus, k and m , and the weak link strength and velocity, α and Ω , is somewhat convoluted and not shown here. For more details, we refer to Appendix and Ref. [35].

The full energy spectrum of dragged solitons in the link's frame of reference is plotted in Fig. 1 for reduced 1D couplings $g = -1, 0, 1$ and delta strengths $\alpha = 0, \frac{1}{8}, \frac{1}{4}$. The general solution has the form of a moving gray solitonic train, which may become a dark solitonic train at $\Omega = n, \frac{n}{2}$, with n integer (black dots in Fig. 1), or plane waves in the absence of a link, at $\alpha = 0$ [parabolas in Figs. 1(a), 1(d) and 1(g)]. This spectrum is characterized, for either attractive or repulsive condensates, by a set of concatenated swallowtail diagrams, each forming an energy band corresponding to solutions with a different number of solitons, indicated by different colors

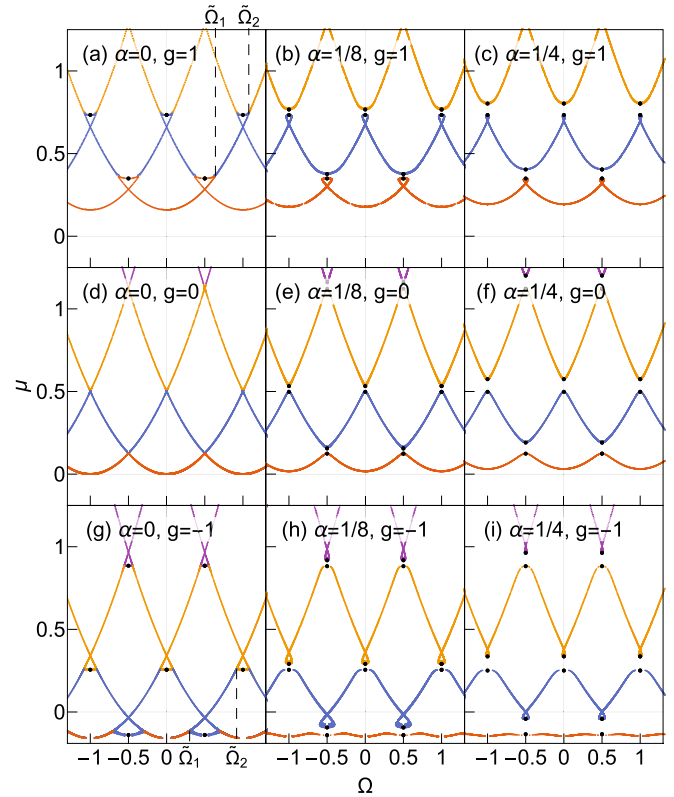


FIG. 1. Spectrum of energies μ of solitonic solutions moving at constant velocity Ω , in the frame of reference of the moving waves and/or link. Left-hand side plots correspond to free solutions on a ring. The parabolas centered at $\Omega = 0$ in (a), (d), and (g) correspond to the energy of the ground state as observed in the frame of reference moving at Ω . The other parabolas are the energies of vortex states in the same frame of reference. The flat lines crossing among parabolas in each of these plots correspond to gray solitonic trains, where the bottom ones correspond to densities with a single dip, and each upper line to a solitonic train with one more dip in the density. Middle and right-hand side columns correspond to energies of solitonic trains dragged by a link of strengths $\alpha = \frac{1}{8}$ and $\frac{1}{4}$. Each set of concatenated swallowtails is plotted in a different color. Red, blue, and orange bands (first, second and third from the bottom) correspond to solitonic trains with one, two, and three dips in the density. The plots in the middle column continuously turn into the left column ones as α decreases to zero. The colors in the left panels and the velocities $\tilde{\Omega}_1, \tilde{\Omega}_2$ indicate how solutions are split into separate bands if a weak link is turned on, i.e. how they are coupled to the middle and right plots through a variation of α . Solid black dots correspond to dark solitonic trains, where the density minima are zero. Units are dimensionless, with $R = M = \hbar = 1$.

(shades of gray) in Fig. 1. These energy levels only cross for $\alpha = 0$. In this case, the parabolas correspond to plane waves, and represent the energies of vortex states from the point of view of an observer moving at Ω . The lines crossing among these parabolas correspond to gray solitons freely moving at Ω .

The spectrum of dragged solutions for attractive and repulsive condensates differ qualitatively in two main ways. Firstly, for $g < 0$, swallowtails point upward, while for $g > 0$ they

point downward. This implies that a given stirring protocol produces solutions with a different number of solitons in repulsive and attractive condensates. Secondly, the band formed by the ground states at different Ω for $g < 0$ and $\alpha > 0$, plotted as the red (bottom, light gray) line in Figs. 1(h) and 1(i), contains no swallowtail structure and forms a continuous set of solutions. Since these solutions correspond to the ground state of the condensate for each velocity, they are also stable against Bogoliubov perturbations. This means that, in attractive condensates, solutions with one gray soliton, i.e., the dip created by the link, and with largely different currents can be coupled among them through a simple adiabatic variation of the velocity of the link, Ω .

Each set of concatenated swallowtails contains top parts and bottom parts. Each of these parts defines a set of solutions which are continuously connected through a variation of Ω , and is limited by a pair of velocities which mark the tips of the tails (loops) in each diagram, and which we call critical velocities. Note that these critical velocities defined here are not the same as the critical velocity of the fluid which is given by its local speed of sound. Beyond these velocities, stationary solutions for the corresponding band do not exist, and the condensate is not able to sustain solitons comoving with the link. Moreover, these velocities mark the point at which top part and bottom part solutions merge, indicating also instability with respect to Bogoliubov perturbations [39]. This was explicitly found for repulsive condensates, where the top parts were found to be unstable through a Bogoliubov analysis, implying that the stable solutions from the bottom part also become unstable at the critical velocity, where they merge with the unstable ones [35]. In the current production mechanisms discussed in the following, the Bogoliubov analysis is not as relevant for attractive condensates. In this case, hysteresis cycles do not exist, and adiabatic excitation is possible through paths that include only ground states of the corresponding Hamiltonians, which are stable by definition, see Secs. III B and III C.

The critical velocities are computed through Eqs. (2)–(4). In the limit $\alpha \rightarrow 0$ and for $g \neq 0$, where plane wave and gray solitonic solutions merge, these velocities have a simple analytical form given by

$$\Omega_c = \pm \tilde{\Omega}_n \pm l, \quad (6)$$

with $\tilde{\Omega}_n = \sqrt{\frac{g}{2\pi} + \frac{n^2}{4}}$ and with two integers $n > 0$ and $l \geq 0$ [35]. As the barrier strength increases, the critical velocities Ω_c monotonically decrease. In the limit $\alpha \rightarrow \infty$, where gray solitons become fully formed dark solitons with their corresponding phase jump and zero valued density dip, Ω_c converge to a value of $\pm \frac{n}{2} \pm l$.

The spectrum plotted in Fig. 1 is then essential to qualitatively understand how to avoid critical velocities and particular states such as dark solitonic trains when stirring the condensate. This is useful for a better control of the condensate in processes with stirring or moving defects, such as the proposed atomic superconducting interference device [10]. It also shows that if an impurity or a link is set at half integer velocity, pairs of dark solitonic solutions separated by a narrow gap appear in the spectrum. Some of these dark solitonic states are found unstable with respect to perturbations in the

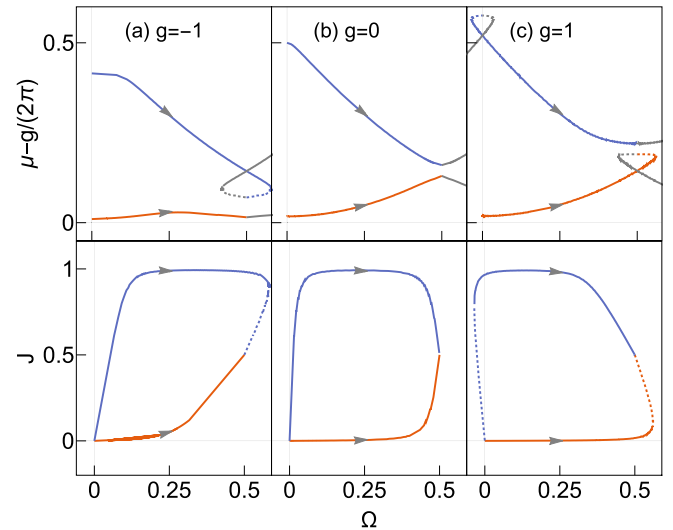


FIG. 2. Current and energy evolution as the ground state in red (bottom line, light gray), and first excited state with two gray solitons in blue (top, dark gray), are stirred with a link of $\alpha = \frac{1}{8}$ and velocities up to $\Omega \simeq 0.5$, and nonlinearities $g = -1, 0, 1$. Dashed lines correspond to the bottom and top parts of upward and downward swallowtail diagrams. The gray (right) lines in top plots are included to better visualize the swallowtail structure. All units are in terms of $R = M = \hbar = 1$.

condensate through a Bogoliubov analysis [35], and are also shown to trigger phase slips [20]. Finally, Fig. 1 also illustrates how the different excited states can be coupled among them and to the ground state by tuning the link strength α and velocity Ω , providing a basis to study hysteresis cycles. We illustrate a sample of such stirring protocols in the following sections.

III. CURRENT PRODUCTION

The current, $J = -\frac{i}{2} \int d\theta (\phi^* \phi' - \phi \phi'^*)$, for a link modeled by a Dirac delta, is given by

$$J = \pm 2\pi \gamma + n, \quad (7)$$

with n an integer, and

$$\gamma = \frac{1}{g(2\pi)^{3/2}} \sqrt{g + k\eta} \sqrt{g - 2\pi k^2 + k\eta} \times \sqrt{g - 2\pi k^2(1 - m) + k\eta}. \quad (8)$$

Together with $\alpha(k, m)$ and $\Omega(k, m)$, the current can be found in terms of α and Ω by scanning the well defined parameter space given by the frequency $k \geq 0$ and elliptic modulus $m \in [0, 1]$, as done with the chemical potential. The analytical results shown in the following plots are corroborated by simulations of the time-dependent GPE in the laboratory frame, where a peaked Gaussian potential explicitly moves around the ring. Solutions from both methods are found to overlap for Gaussian amplitude widths $\sigma = 2\pi/200$.

A. Adiabatic, regular stirring

Figure 2 shows the current evolution for three different cases, $g = -1, 0, 1$, as a link is set on the ground (red line/bottom one with lighter shade) and first excited (blue line/second and darker one) state and then stirred by adiabatically increasing the velocity from $\Omega = 0$ to $\Omega \simeq 0.5$.

For $g < 0$, a link can be set in the ground state and its velocity increased indefinitely. The current can be steadily increased, and the solutions alternate between a shallow gray soliton moving at $\Omega = n$ and a dark soliton moving at $\Omega = n + \frac{1}{2}$. See the red (bottom, light gray) lines in Fig. 2(a) for the energy and current evolution in the path $\Omega = 0 \rightarrow 0.5$. This current is produced more abruptly for attractive interactions closer to zero. For weak interactions, $g \lesssim 0$, the first excited state consists in two dark solitons, with $J = 0$. When this state is stirred, a current $J \simeq 1$ in the stirring direction is produced at very small velocities, and then is kept roughly constant up to the critical velocity, $\Omega_c \gtrsim 0.5$, see the blue (top, dark gray) line in Fig. 2(a). See also Fig. 6 for the densities of the ground and first excited states at $\Omega = 0, 0.5$.

For the repulsive case, stirring the ground state with increasing velocity leaves the current practically constant, and a critical velocity is found at $\Omega \gtrsim 0.5$, $\Omega \in (0.5, \tilde{\Omega}_1)$, as shown in Fig. 2(c) (red/bottom line). This velocity marks the tip of the lowest and right swallowtail, and is connected to the solution with one dark soliton through a set of unstable solutions [35]. The first excited state corresponds to the first vortex state and for $\alpha \gtrsim 0$ contains two gray solitons. Its energy is represented by the crossing blue and gray (upper) lines in Fig. 2(c). In the limit $\alpha \rightarrow 0$, it turns into a plane wave with one unit of angular momentum. If this vortex is stirred, the current remains roughly constant for small velocities, and rapidly decreases to $J = 0.5$ at $\Omega \lesssim 0.5$.

The linear case, $g = 0$, in panel (b) of Fig. 2, presents similar current dynamics, except that initial states are all static ($J = 0$), and no critical velocities are encountered in any stirring. In this case, link velocities can be increased and decreased indefinitely.

The adiabatic paths described above can also be understood in reverse, that is, in terms of a decreasing stirring velocity. Moreover, we note that, due to rotational symmetry, the evolution of the currents of these paths is also valid for the same states and stirrings but with velocities $\Omega \rightarrow \pm\Omega + n$ and currents $J \rightarrow \pm J + n$, with n an integer.

B. Adiabatic, excitation stirring

The stirring procedures of Fig. 2, consisting in a steady increase of the link's velocity up to $\Omega \simeq 0.5$, allow us to produce currents $|\Delta J| \lesssim 1$. Passed these velocities, critical velocities are encountered, and the condensate cannot be adiabatically excited anymore. However, there are cases where critical velocities are not a limitation. In particular, the ground state of attractive condensates, any state for the linear case, and in general dark solitonic states in the limit $\alpha \rightarrow \infty$, where the tails in the energy spectrum shrink and vanish. These states can be continuously excited to states with larger currents by constantly increasing the velocity of the link.

We follow similar procedures in attractive and repulsive condensates that couple the ground state to excited states so

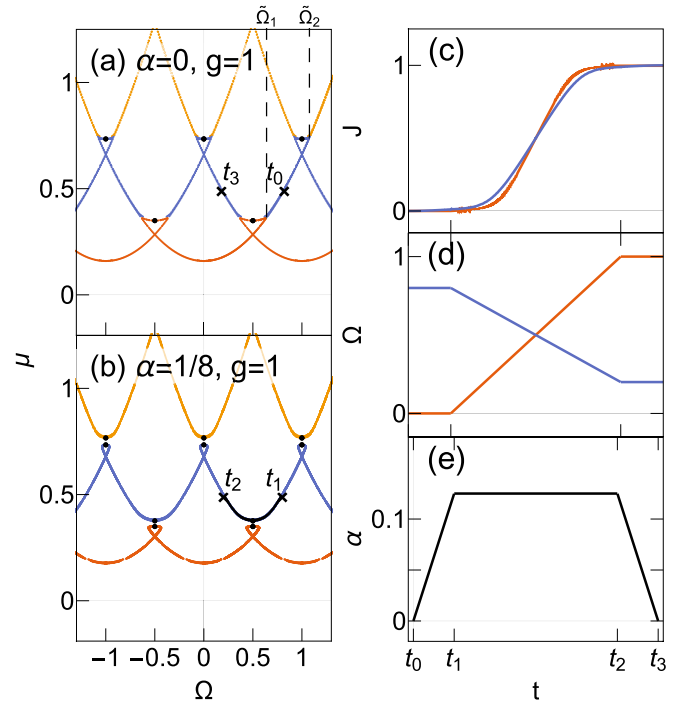


FIG. 3. Spectrum of energies for $g = 1$ in the absence of a link (a) and with a link of $\alpha = \frac{1}{8}$ (b), together with the key points in the adiabatic path to excite the condensate to current $J = 1$. Points t_0 and t_3 correspond to the ground state and first vortex state in the reference frame of an observer moving at $\Omega_i \in (\tilde{\Omega}_1, \tilde{\Omega}_2)$, and $\Omega_f = -\Omega_i + 1$. Points t_1 and t_2 , and the path uniting them, consist of solutions with two gray solitons being dragged by the link. On the right-hand side plots we show in blue the evolution of the current (c) and link velocity (d), and in black the link strength (e) between times t_0 and t_3 . Exciting attractive condensates from the ground state also involves setting and unsetting a link as in plot (e). In this case, the link is set at zero velocity and then increased [red/light-gray line in plot (d)], the current evolving similarly as for the repulsive condensate [red/light-gray line in plot (c)]. All quantities are in natural units.

that $|\Delta J| \geq 1$. For repulsive condensates, a link is set in the ground state while rotating at a velocity Ω_i . Initial velocities $\Omega_i \in (\tilde{\Omega}_n, \tilde{\Omega}_{n+1})$ access the n th excited state, i.e., the one with $n + 1$ solitons. The velocity is then decreased down to the other side of the swallowtail diagram, and then the weak link is turned off. These cycles include an intermediate dark solitonic solution (with $n + 1$ dark solitons), and the current increases more abruptly in the middle points of the paths. An example of such cycles that excites the repulsive condensate to $J = 1$ is shown in Fig. 3. At time t_0 , an observer is rotating at $\Omega_i \in (\tilde{\Omega}_1, \tilde{\Omega}_2)$ around the ground state. As this observer sets a link while moving at Ω , at point t_1 , two dips in the density are created moving at the same velocity, one at the link's position and another in the opposite site. As the velocity is decreased, the dips become deeper, forming a dark solitonic train at $\Omega = 0.5$, and returning to the original gray solitonic train at t_2 . At this point, however, the link and gray solitons are moving much slower and the condensate current is close to $J = 1$. By removing the slowly moving weak link, we recover the free and flat condensate, now with a current $J = 1$, at point t_3 .

Attractive states with $g \lesssim 0$ allow for two possible excitation processes. Firstly, and analogously to the repulsive case, a link can be set at a finite velocity Ω_i . Initial rotations $\Omega_i \in (\tilde{\Omega}_n, \tilde{\Omega}_{n+1})$ produce solutions corresponding to the n^{th} excited state. In this case, the velocity must be *increased* up to the following swallowtail diagram, such that critical velocities are avoided, see Fig. 1. Secondly, and perhaps more naturally, we can stir by setting a link at zero velocity, and then speed up the stirring. This process takes advantage that no critical velocities are encountered when stirring the ground state of attractive condensates. Removing the link at $\Omega = n$ will then produce vortex states with n quanta of angular momentum. The evolution of the current up to $J = 1$, and of the link's velocity and strength corresponding to this protocol, are plotted in Figs. 3(c)–3(e).

We have focused our attention to $|g|$ small enough such that for attractive condensates the ground state is always coupled through the stirring strength and velocity to all other states. This is not the case at $g \ll 0$ (see Appendix), where new types of solutions appear. In this case, the ground state does not have a flat density. It can be stirred with increasing velocity, analogously to the above excitation processes, but the final states are also not flat.

Note that in this section we considered the adiabatic following of particular eigenstates of the system. That is, we assume that the adiabaticity condition is fulfilled and no other eigenstates are populated during the stirring [40]. In particular, if we consider only the closest energy eigenstates of the system, the adiabatic condition will depend on the gap opened by the barrier. This is particularly important around the swallowtails where the gap is small. In a simplified two-state model the adiabaticity condition can be calculated analytically and is given by $\frac{1}{2} \left| \frac{d\lambda}{dt} \Delta E - \lambda \frac{d\Delta E}{dt} \right| \ll (\lambda^2 + \Delta E^2)^{3/2}$ [41,42], with ΔE being the energy difference between eigenstates and λ the tunneling amplitude between the two states.

C. Hysteresis cycles

Hysteresis due to a rotating weak link in a Bose gas was first experimentally observed in [6]. These hysteresis cycles are understood in terms of (downward) swallowtail diagrams [39], and their widths were numerically computed in [26]. Here we discuss how for a delta type link the widths and heights of the hysteresis cycles, $\Delta\Omega$ and ΔJ , can be computed using the exact spectrum presented in this work. Our simplified 1D GPE model thus yields a minimal expression of the hysteresis results found in Ref. [6], providing insight into the fundamental hysteresis mechanism from a more analytical point of view. In this experimental setup, a blue-detuned laser beam creates an effective repulsive potential, which is rotated or stopped around the ring trap to create or destroy currents. We follow an analogous protocol through cycles which contain adiabatic excitation paths and spontaneous decay. The adiabaticity condition, discussed previously, is related to the energy gap between the present state and the closest energy eigenstate, which in turn depend on the weak link strength. This condition does not represent a major limiting factor in these experiments, in which the barrier strength can be tuned to increase or decrease the energy gaps. Differences between

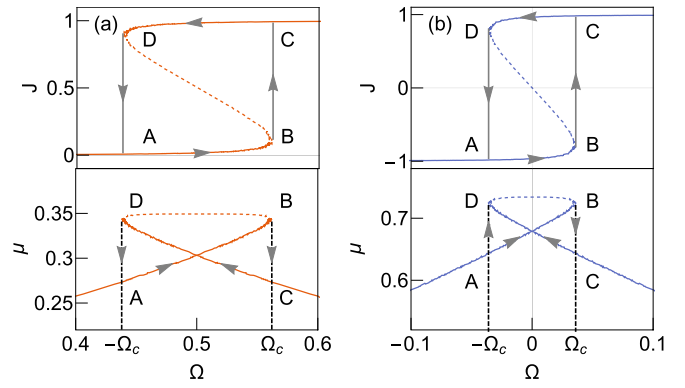


FIG. 4. Hysteresis cycles in terms of currents and stirring velocities (top plots) and corresponding energy diagrams in form of swallowtails (bottom plots) for $\alpha = \frac{1}{8}$. (a) Stirring of the ground state up to Ω_c , $A \rightarrow B$, transition to $J \simeq 1$ through the gray line (vertical arrow), $B \rightarrow C$, and stirring in opposite direction, $C \rightarrow D$, where the condensate decays to the original state, $D \rightarrow A$. (b) When a link is set in a vortex state, two solitons are produced, but the hysteresis paths are analogous to the ground state case. In this cycle, the paths are cut short at much smaller critical velocities. μ , J , and Ω are in natural units.

1D GPE results and experiments, typically performed in 3D setups where transverse excitations can play a substantial role, might still appear. Our model, however, is capable of describing some of the main qualitative features found in experiments.

Figure 1 proves useful to illustrate the main features of hysteresis. On the one hand, it shows that only repulsive condensates present downward swallowtail structures, and therefore the associated hysteresis cycles only exist for $g > 0$. This is because when the critical velocity is reached at the tip of an upward swallowtail, the state with lower energy to which the condensate decays belongs to a lower set of concatenated swallowtails. This effectively impedes to excite the condensate back to the upper swallowtail through any adiabatic variation of Ω , and therefore to close the cycle. On the other hand, hysteresis cycles on repulsive condensates are not characteristic of a stirring of the ground state, where the condensate undergoes a transition $\Delta J \simeq 1$. Stirring of excited states also present hysteresis, each excited state implying a different width $\Delta\Omega$ and height ΔJ , features not discussed in previous works. Moreover, these cycles can be analyzed in terms of the nonlinearity and link's strength. In general, the range of velocities limited by Ω_c , and the associated adiabatic widths of the swallowtails and hysteresis cycles, $\Delta\Omega$, become smaller as larger transitions ΔJ are considered, as g decreases, or as the link's magnitude α becomes stronger. This qualitatively agrees with the experimental results found in Fig. 3 of Ref. [6], where the bottom and top widths of the cycles, in which the current varies slightly, and the critical velocities decrease as stronger barriers are considered. On the other hand, the precise dependence of the current on the velocity in the nonadiabatic transitions, in which the current is observed to increase more abruptly, is beyond the scope of our model. In the limit $\alpha \rightarrow 0$, the heights and widths of the cycles become $\Delta J = n$, $\Delta\Omega = 2\tilde{\Omega}_n - n$, with integer n .

In Fig. 4, we present two hysteresis cycles, one corresponding to stirring the ground state, where $\Delta J \simeq 1$, and another associated to setting a link in a vortex state, and then stirring, effectively coupling $J \simeq -1$ and $J \simeq 1$ vortex states. Both cycles involve adiabatic paths in which the condensate is stirred up to the corresponding critical velocity. Passed these velocities, the condensate is assumed to decay to the next vortex state, that is, to the lower branch of the same swallowtail structure, increasing the current in roughly one and two units of angular momentum, respectively. Note that these paths, shown in gray (vertical arrows) in Fig. 4, are plotted straight and vertically, just to assume the simplest case. Then the condensate is stirred in the opposite direction, where the same process is repeated, returning thus to the original state. The critical velocities limiting the stirring of the ground state are found to coincide with $\sqrt{g\rho_0}$, where ρ_0 is the density at the lowest point, as in Ref. [26]. For excited states, however, these velocities slightly depart from the sound velocity at the low density region.

In Ref. [35], an extensive discussion on the stability of swallowtail diagrams was performed, including a precise formula to compute the critical velocities. Solutions constituting the upper parts of swallowtails were found unstable with respect to Bogoliubov perturbations, while the lower parts of the ground and first excited state were fully stable for repulsive links. This implies that the initial paths of these hysteresis cycles, corresponding to the lower part of the swallowtails, constitute a set of stable solutions. Once the tip of the swallowtail is reached through the lower part, and a critical velocity is encountered, the set of stable solutions merges with the set of unstable ones. At this point, the condensate undergoes a nonadiabatic transition towards the other lower branch of the swallowtail. The precise dynamics of these instabilities is beyond the capabilities of the current model. However, knowing the precise values of the critical velocities, and the corresponding solutions in terms of elliptic functions, might allow for an easier identification of the physical mechanisms behind the bifurcation instabilities, with either finite temperature, time-dependent computations [43,44], or through more general instability criteria such as the enhancement of dynamical density fluctuations [45,46].

D. Auxiliary potential and phase imprinting

The adiabatic paths presented so far involve the movement of the link or a stirring. An alternative procedure to excite the condensate is to imprint a phase through an electromagnetic field [19]. Phase imprinting provides a fast way to excite the condensate, but when the ring contains a static defect, which might happen naturally in experiment, the state obtained is not stationary, and one encounters BJJ oscillations [20], or other nonlinear effects if g is large enough. These oscillations can be understood intuitively through simplified hydrodynamics considerations. If a linear phase is imprinted, all the atoms throughout the annular trap acquire the same momentum, which implies a smaller current at the low density region created by the defect. The condensate thus accumulates at the side of the defect, slows down, and bounces to the other side of the barrier. This effect can be partially reduced by imprinting a nonlinear phase such that a larger kick is provided to

the condensate at the low density region, producing thus a current which is roughly stationary, i.e., $J(\theta) = \rho(\theta)\beta'(\theta) \simeq$ constant. This idea can be quantitatively analyzed since the excited stationary states with current $J \simeq n$ and a delta defect are well known in terms of Jacobi elliptic functions. One can in principle imprint the phase of these states on the ground state, but the unperturbed density would still differ from the densities of stationary ones, which, apart from the dip produced by the link, contain other gray solitons. Therefore the final states would not be stable. To solve this, and taking advantage of adiabatic processes, we design a protocol to produce the density of the desired excited state through an auxiliary potential [47,48], and leaving the link fixed. Once this condensate's density is obtained, the phase is imprinted and the auxiliary potential is turned off.

More explicitly, if the final stationary solution we want to obtain, in presence of the delta potential, is $\psi_s(\theta) = r_s(\theta)e^{i\beta_s(\theta)}$, we first set an auxiliary potential V_{aux} such that the ground state is $\psi_g = r_s(\theta)$, and therefore satisfies

$$\tilde{\mu}r_s = -\frac{1}{2}r_s'' + gr_s^3 + V_{\text{aux}}r_s. \quad (9)$$

On the other hand, the final excited state we want to build is determined by

$$\mu r_s = -\frac{1}{2}[r_s'' - r_s\beta_s'^2 + i(r_s\beta_s'' + 2r_s'\beta_s')] + gr_s^3. \quad (10)$$

The imaginary part is zero as long as $\beta_s' = \frac{\gamma}{r_s^2}$, with γ being a constant representing the current. Subtracting both equations, and neglecting the constant $\tilde{\mu} - \mu$, we find

$$V_{\text{aux}}(\theta) = \frac{1}{2}\beta_s'(\theta)^2 = \frac{\gamma^2}{2r_s(\theta)^4}. \quad (11)$$

The protocol then consists in gradually turning on $V_{\text{aux}}(\theta)$, for example by increasing its overall factor from zero to one, and then turn it off while phase imprinting $\beta_s(\theta)$. The stationary state $r_s(\theta)e^{i\beta_s(\theta)}$ with current $J \simeq n > 0$ is thus accessed.

This protocol is reproduced through simulations in the time-dependent GPE, as shown in Fig. 5, obtaining a steady current $J \simeq 1$. This is in contrast with regular phase imprinting, which for large enough defects, in our tested case $\alpha = 0.3$, produces BJJ oscillations, as also shown in the figure. Apart from the protocol described above, we study the evolution of the current when only the auxiliary potential is used—only the density of the stationary current with a delta is imitated, and a regular slope is imprinted—and when only the nonlinear phase imprinting is used on the ground state with a delta. We observe that in all cases, both the auxiliary potential and the nonlinear phase imprinting, serve independently to produce more self-trapping in the final state.

IV. CONCLUSIONS

We have described the spectrum of solitons moving at constant velocity in a ring condensate, either freely, or being dragged by a weak link, and with either attractive or repulsive interactions. Their energies, densities, and currents have been thoroughly analyzed in terms of the link's strength α and velocity Ω , and found that all states are coupled at $\alpha = 0$. At $\alpha \neq 0$, the steady dragged solitonic solutions exist only in certain ranges of link velocities, periodic in Ω , and the midpoints

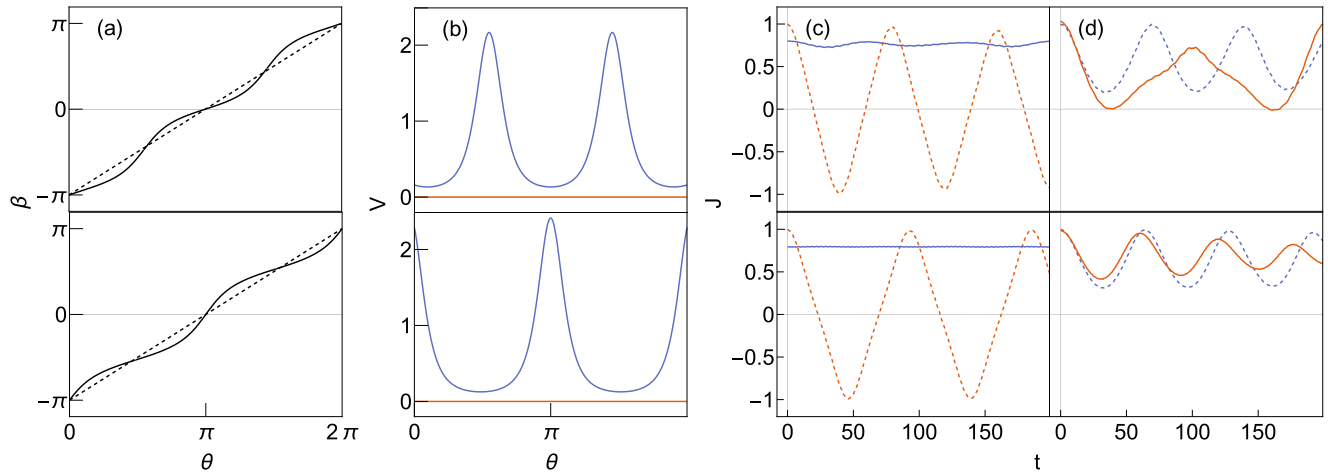


FIG. 5. Top plots correspond to $g = -1$ and bottom ones to $g = 1$. (a) Linear (dashed lines) and nonlinear ($\beta_s(\theta)$, solid lines) phases. (b) Auxiliary potential $V(\theta) = V_{\text{aux}}(\theta)$ (blue/upper line) and $V(\theta) = 0$ (red/lower line). (c) Current evolution after regular phase imprinting (dashed red), and after applying the auxiliary potential and imprinting the nonlinear slope (solid blue). The protocol is carried out on the ground state of the GPE with a link of strength $\alpha = 0.3$. (d) Intermediate cases in which only the auxiliary potential (dashed blue) or the nonlinear phase imprinting (solid red) are used. Units are dimensionless with $R = M = \hbar = 1$.

of which, at integer and half-integer velocities, correspond to dark solitonic states.

By studying how the different stationary states are connected through an adiabatic variation of α and Ω , we have laid out three different methods to modify the state of the condensate in a controlled manner. The first, involves a purely adiabatic variation of the link's strength and velocity. Setting a link and then stirring by increasing its velocity, allows to excite the ground state of attractive condensates, but in all other cases critical velocities are encountered, and current variations are limited to $|\Delta J| \lesssim 1$. To access excited states, the link must be set while rotating at a finite velocity. Secondly, we have considered processes in which the link moves but its strength is kept fixed. In this case, the link's velocity surpasses the critical one and the condensate is assumed to decay to the immediate lower state. For repulsive condensates, these paths, consisting in both an adiabatic excitation part and a nonadiabatic decay, can be closed by moving the weak link in both directions, and effectively producing hysteresis cycles. Here, we have shown that these hysteresis cycles can also be produced in excited states, although they are limited by different critical velocities, and that hysteresis cycles cannot exist for attractive condensates. Finally, we have made use of an auxiliary potential to adiabatically modify the ground state density, and to then imprint a nonlinear phase while the potential is turned off. The auxiliary potential and phase are precisely designed such that the state produced is an excited but stationary state, and no BJJ oscillations are found.

This work illustrates, from an analytical point of view, the physical mechanisms involved in the production of currents in weakly interacting Bose gases in a ring trap. It also provides a theoretical description which allows for further exploration of the system, including ground states as well as excited states.

ACKNOWLEDGMENTS

A.P.-O. and T.C. acknowledge the support by KUT presidential grant at Research Institute, Kochi University of

Technology, Japan. J.P. acknowledges Okinawa Institute of Science and Technology Graduate University and also the JSPS KAKENHI Grant Number 20K14417.

APPENDIX: SPECTRUM

The spectrum of normalized solutions is more easily analyzed in the delta comoving frame, which is determined by Eqs. (2)–(4). The solutions of these equations are parametrized through a density ρ and a phase β , $\phi(\theta) = \sqrt{\rho(\theta)}e^{i\beta(\theta)}$, and are given in analytical form in terms of Jacobi elliptic functions (F), $\rho(\theta) = A + BF^2(k(\theta - \theta_0), m)$, and where $\rho(\theta)\beta'(\theta) = \gamma$ is constant. In our case, we set the Jacobi function $F = dn$. A , B , and θ_0 depend on the frequency $k \geq 0$ and elliptic modulus $m \in [0, 1]$. $\rho(\theta)$ in general oscillates around a finite value, has no zeros, and is smooth except for the derivative jump due to the delta at $\theta = 0$. In the limits $A \rightarrow 0$ and $B \rightarrow 0$, these solutions become dark solitons and plane waves, respectively. In the following we illustrate the main features of the spectrum according to Fig. 1.

In the linear and free case, $g = 0$ and $\alpha = 0$, the solutions are plane waves or vortex states, with the chemical potential quantized by periodic conditions and given by $\mu = \frac{n^2}{2}$. Each parabola in Fig. 1(d) represents the energy of each of these states, $\mu = \frac{1}{2}(\Omega + n)^2$, as measured by an observer moving around the ring at constant velocity Ω . In the laboratory frame each parabola represents the same solution with energy $\frac{n^2}{2}$.

When atomic interactions are finite, $g \neq 0$, and no link is present, $\alpha = 0$, the condensate is governed by the GPE with periodic boundary conditions, which also has as solutions plane waves. Their energy includes the same kinetic term as in the linear case, but also a potential term which shifts the energy parabolas upward and downward for the repulsive and attractive cases, $\mu = \frac{g}{2\pi} + \frac{1}{2}(\Omega + n)^2$. Moreover, there are new sets of solutions, consisting in gray solitons moving at constant velocity Ω . Their energies as a function of Ω , in the frame of reference of the moving solitons, are shown in Figs. 1(a) and 1(g) as the curves crossing between the

plane wave parabolas. The middle points of these crossing lines, marked as black dots, correspond to dark solitons. Even number of dark solitons move at velocities $\Omega = n$, while odd number of dark solitons travel at $\Omega = n + \frac{1}{2}$, with n an integer. These waves are always nonmoving with respect to the condensate. As the gray solitons become shallower, their velocities depart from $\Omega = n, n + \frac{1}{2}$, until the densities become completely flat and these solutions merge with the plane waves. These sets of solutions can be understood as energy bands in the laboratory frame. Each band consists in solutions with a fixed number of solitons with velocities ranging from m to $\Omega = m \pm n$. A more rigorous analysis of the first band of gray solitonic solutions can be found in Ref. [49].

The energies of the gray solitons increase and decrease with g , and this implies the appearance of new static solutions ($\Omega = 0$) as $|g|$ grows larger [28], in particular of new ground states for $g < 0$. In this article we have focused on $|g|$ small enough so that the ground state for attractive condensates stays coupled to the rest of the spectrum. To illustrate how the spectrum qualitatively depends on g , we consider two particular cases, one for attractive condensates and one for repulsive ones. First, as g decreases from $g = 0$, the lowest of these crossing lines [blue lines in Fig. 1(g)] move downward, until their left and right limits coincide with the bottom points of the parabolas, at $\tilde{\Omega}_1 = 0, g = -\frac{\pi}{2}$. For $g < -\frac{\pi}{2}$, the ground state as a function of Ω forms a continuous line uncoupled from the rest of parabolas. In general, new uncoupled states appear at $g < -\frac{n\pi}{2}$, with integer $n > 0$. Another example is the appearance of a new second excited state as g grows and the red solitonic line in Fig. 1(a) crosses the axis $\Omega = 0$. More precisely, at $g = \frac{3\pi}{2}$, such that the left limit coincides with the vertical axis, $1 - \tilde{\Omega}_1 = 0$, a new solution appears at $\Omega = 0$ between the first vortex state and the first dark solitonic solution.

As a link is turned on, $\alpha > 0$, the spectrum of plots (a), (d), and (g) described above splits into a set of diagrams separated by a gap. For finite g , these diagrams have the shape of downward ($g > 0$) and upward ($g < 0$) swallowtails. The gap among the swallowtails grows for larger delta strengths and nonlinearities. Each set of concatenated swallowtail diagrams represents a set of solutions with a fixed number of solitons. The densities of the lowest set of swallowtails have only the downward kink created by the delta. Then, each superior set has, apart from the dip in the density produced by the link, one more gray soliton. The middle points of these diagrams still represent dark solitons, each previous dark solitonic solution at $g = 0$ now split into two. In the solution with higher energy,

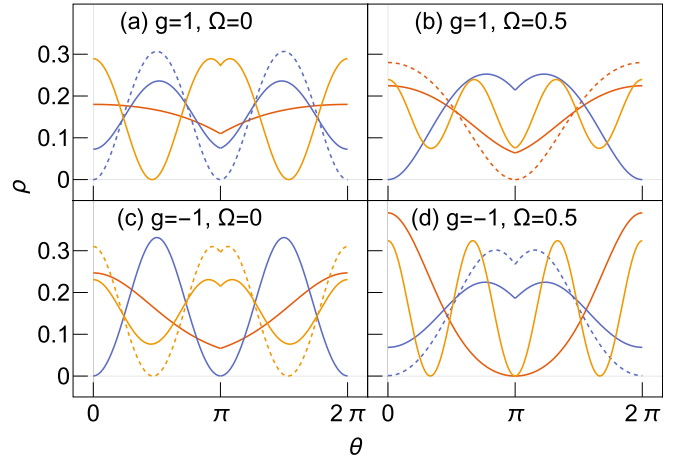


FIG. 6. Densities for the ground state and first excited states given a link of strength $\alpha = \frac{1}{4}$ and velocities and nonlinearities $g = \pm 1, \Omega = 0, 0.5$. Colors (shades of grey) match the ones of their respective energies in Fig. 1, and dashed lines correspond to upper parts of downward swallowtails, or bottom parts of upward ones. In this figure, the delta is placed at $\theta = \pi$ for visualization purposes. In the rest of the article the delta conditions are at $\theta = 0, 2\pi$. All units are dimensionless and $R = M = \hbar = 1$.

the dark soliton coinciding with the delta corresponds to a derivative jump, satisfying delta conditions. The solution with lower energy consists in a periodic and smooth wave such that one of the zeros coincides with the position of the link. Solutions of this type trivially satisfy delta conditions for any α , since the derivatives and the function at the position of the delta are zero. In Fig. 1, this means the black dots in the red lines, the ones in the blue lines at $\Omega = n$, and the ones at the orange lines at $\Omega = n + \frac{1}{2}$, have the same μ across the panels in each row. As a sample, the densities of these pairs of dark solitonic trains, and the ground and other excited states, are plotted in Fig. 6 for $\alpha = \frac{1}{4}, g = -1, 1$ and $\Omega = 0, 0.5$.

We herewith have thoroughly described the set of solitonic solutions in correspondence to Fig. 1. To sum up, the solutions for $\alpha = 0$ consist of vortex states with current $J = n$, of m dark solitons moving at $\Omega = \frac{m}{2} + n$, and of m gray solitons traveling at $\Omega \in (\frac{m}{2} + n - |\tilde{\Omega}_m - \frac{m}{2}|, \frac{m}{2} + n + |\tilde{\Omega}_m - \frac{m}{2}|)$, with integers n, m . For a rotating link, the dragged solutions comprise trains with $m + 1$ gray solitons coupling solutions with m and $m + 1$ dark solitons moving at $\Omega = \frac{m}{2} + n$ and $\Omega = \frac{m}{2} + n + \frac{1}{2}$, respectively, and limited by critical velocities Ω_c .

-
- [1] L. Amico, G. Birkel, M. Boshier, and L.-C. Kwek, *New J. Phys.* **19**, 020201 (2017).
 [2] C. Ryu, M. F. Andersen, P. Cladé, V. Natarajan, K. Helmerson, and W. D. Phillips, *Phys. Rev. Lett.* **99**, 260401 (2007).
 [3] S. Moulder, S. Beattie, R. P. Smith, N. Tammuz, and Z. Hadzibabic, *Phys. Rev. A* **86**, 013629 (2012).
 [4] S. Beattie, S. Moulder, R. J. Fletcher, and Z. Hadzibabic, *Phys. Rev. Lett.* **110**, 025301 (2013).
 [5] K. C. Wright, R. B. Blakestad, C. J. Lobb, W. D. Phillips, and G. K. Campbell, *Phys. Rev. A* **88**, 063633 (2013).
 [6] S. Eckel, J. G. Lee, F. Jendrzejewski, N. Murray, C. W. Clark, C. J. Lobb, W. D. Phillips, M. Edwards, and G. K. Campbell, *Nature (London)* **506**, 200 (2014).
 [7] C. Ryu, P. W. Blackburn, A. A. Blinova, and M. G. Boshier, *Phys. Rev. Lett.* **111**, 205301 (2013).
 [8] D. W. Hallwood, T. Ernst, and J. Brand, *Phys. Rev. A* **82**, 063623 (2010); D. Solenov and D. Mozyrsky, *ibid.* **82**, 061601(R) (2010); A. Nunnenkamp, A. M. Rey, and K. Burnett, *ibid.* **84**, 053604 (2011); D. Solenov and D. Mozyrsky, *J. Comput. Theor. Nanosci.* **8**, 481 (2011).

- [9] C. Schenke, A. Minguzzi, and F. W. J. Hekking, *Phys. Rev. A* **84**, 053636 (2011).
- [10] L. Amico, D. Aghamalyan, F. Auzshtol, H. Crepaz, R. Dumke, and L.-C. Kwek, *Sci. Rep.* **4**, 4298 (2014).
- [11] J. Hou, X.-W. Luo, K. Sun, and C. Zhang, *Phys. Rev. A* **96**, 011603(R) (2017).
- [12] Y. Guo, R. Dubessy, M. G. de Herve, A. Kumar, T. Badr, A. Perrin, L. Longchambon, and H. Perrin, *Phys. Rev. Lett.* **124**, 025301 (2020).
- [13] K. C. Wright, R. B. Blakestad, C. J. Lobb, W. D. Phillips, and G. K. Campbell, *Phys. Rev. Lett.* **110**, 025302 (2013).
- [14] D. Aghamalyan, M. Cominotti, M. Rizzi, D. Rossini, F. Hekking, A. Minguzzi, L.-C. Kwek, and L. Amico, *New J. Phys.* **17**, 045023 (2015).
- [15] F. Piazza, L. A. Collins, and A. Smerzi, *Phys. Rev. A* **80**, 021601(R) (2009).
- [16] A. Ramanathan, K. C. Wright, S. R. Muniz, M. Zelan, W. T. Hill, C. J. Lobb, K. Helmerson, W. D. Phillips, and G. K. Campbell, *Phys. Rev. Lett.* **106**, 130401 (2011).
- [17] F. Piazza, L. A. Collins, and A. Smerzi, *J. Phys. B: At. Mol. Opt. Phys.* **46**, 095302 (2013).
- [18] J. Dalibard, F. Gerbier, G. Juzeliūnas, and P. Öhberg, *Rev. Mod. Phys.* **83**, 1523 (2011).
- [19] A. Kumar, R. Dubessy, T. Badr, C. De Rossi, M. de Goër de Herve, L. Longchambon, and H. Perrin, *Phys. Rev. A* **97**, 043615 (2018).
- [20] J. Polo, R. Dubessy, P. Pedri, H. Perrin, and A. Minguzzi, *Phys. Rev. Lett.* **123**, 195301 (2019).
- [21] R. Kanamoto, L. D. Carr, and M. Ueda, *Phys. Rev. A* **79**, 063616 (2009).
- [22] O. Fialko, M.-C. Delattre, J. Brand, and A. R. Kolovsky, *Phys. Rev. Lett.* **108**, 250402 (2012).
- [23] Y. Li, W. Pang, and B. A. Malomed, *Phys. Rev. A* **86**, 023832 (2012).
- [24] A. Muñoz Mateo, V. Delgado, M. Guilleumas, R. Mayol, and J. Brand, *Phys. Rev. A* **99**, 023630 (2019).
- [25] S. Baharian and G. Baym, *Phys. Rev. A* **87**, 013619 (2013).
- [26] A. Muñoz Mateo, A. Gallemí, M. Guilleumas, and R. Mayol, *Phys. Rev. A* **91**, 063625 (2015).
- [27] M. Kunimi and Y. Kato, *Phys. Rev. A* **91**, 053608 (2015).
- [28] L. D. Carr, C. W. Clark, and W. P. Reinhardt, *Phys. Rev. A* **62**, 063610 (2000); **62**, 063611 (2000).
- [29] B. T. Seaman, L. D. Carr, and M. J. Holland, *Phys. Rev. A* **71**, 033609 (2005).
- [30] V. Hakim, *Phys. Rev. E* **55**, 2835 (1997).
- [31] N. Pavloff, *Phys. Rev. A* **66**, 013610 (2002).
- [32] M. Cominotti, D. Rossini, M. Rizzi, F. Hekking, and A. Minguzzi, *Phys. Rev. Lett.* **113**, 025301 (2014).
- [33] E. Shamriz and B. A. Malomed, *Phys. Rev. E* **98**, 052203 (2018).
- [34] A. Pérez-Obiol and T. Cheon, *J. Phys. Soc. Jpn.* **88**, 034005 (2019).
- [35] A. Pérez-Obiol and T. Cheon, *Phys. Rev. E* **101**, 022212 (2020).
- [36] M. Kunimi and I. Danshita, *Phys. Rev. A* **100**, 063617 (2019).
- [37] D. A. Takahashi, *Phys. Rev. E* **93**, 062224 (2016).
- [38] B.-F. Feng, L. Ling, and D. A. Takahashi, *Stud. Appl. Math.* **44**, 46 (2019).
- [39] E. J. Mueller, *Phys. Rev. A* **66**, 063603 (2002).
- [40] A. Messiah, *Quantum Mechanics* (North-Holland, Amsterdam, 1976), Vol. 2.
- [41] L. Allen and J. H. Eberly, *Optical Resonance and Two-Level Atoms* (Dover Publications, New York, 1987).
- [42] N. V. Vitanov, T. Halfmann, B. W. Shore, and K. Bergmann, *Annu. Rev. Phys. Chem.* **52**, 763 (2001).
- [43] T. Karpiuk, P. Deuar, P. Bienias, E. Witkowska, K. Pawłowski, M. Gajda, K. Rzazewski, and M. Brewczyk, *Phys. Rev. Lett.* **109**, 205302 (2012).
- [44] G. C. Katsimiga, S. I. Mistakidis, G. M. Koutentakis, P. G. Kevrekidis, and P. Schmelcher, *Phys. Rev. A* **98**, 013632 (2018).
- [45] Y. Kato and S. Watabe, *Phys. Rev. Lett.* **105**, 035302 (2010).
- [46] S. Watabe and Y. Kato, *Phys. Rev. A* **88**, 063612 (2013).
- [47] S. K. Schnelle, E. D. van Ooijen, M. J. Davis, N. R. Heckenberg, and H. Rubinsztein-Dunlop, *Opt. Express* **16**, 1405 (2008).
- [48] K. Henderson, C. Ryu, C. MacCormick, and M. G. Boshier, *New J. Phys.* **11**, 043030 (2009).
- [49] A. Sacchetti, *J. Phys. A* **53**, 385204 (2020).